



HAL
open science

Numerical modelling of grinding in a stirred media mill: Hydrodynamics and collision characteristics

Romain Gers, Éric Climent, Dominique Legendre, Dominique Anne-Archard,
Christine Frances

► To cite this version:

Romain Gers, Éric Climent, Dominique Legendre, Dominique Anne-Archard, Christine Frances. Numerical modelling of grinding in a stirred media mill: Hydrodynamics and collision characteristics. *Chemical Engineering Science*, 2010, 65 (6), pp.2052-2064. 10.1016/j.ces.2009.12.003 . hal-03552707

HAL Id: hal-03552707

<https://hal.science/hal-03552707>

Submitted on 2 Feb 2022

HAL is a multi-disciplinary open access archive for the deposit and dissemination of scientific research documents, whether they are published or not. The documents may come from teaching and research institutions in France or abroad, or from public or private research centers.

L'archive ouverte pluridisciplinaire **HAL**, est destinée au dépôt et à la diffusion de documents scientifiques de niveau recherche, publiés ou non, émanant des établissements d'enseignement et de recherche français ou étrangers, des laboratoires publics ou privés.



Open Archive Toulouse Archive Ouverte (OATAO)

OATAO is an open access repository that collects the work of Toulouse researchers and makes it freely available over the web where possible.

This is an author-deposited version published in: <http://oatao.univ-toulouse.fr/>
Eprints ID: 4496

To link to this article: DOI:10.1016/j.ces.2009.12.003
<http://dx.doi.org/10.1016/j.ces.2009.12.003>

To cite this version:

Gers, Romain and Climent , Eric and Legendre, Dominique and Anne-Archard, Dominique and Frances, C. (2010) *Numerical modelling of grinding in a stirred media mill: Hydrodynamics and collision characteristics*. Chemical Engineering Science, vol. 65 (n° 6). pp. 2052-2064. ISSN 0009-2509

Any correspondence concerning this service should be sent to the repository administrator: staff-oatao@inp-toulouse.fr

Numerical modelling of grinding in a stirred media mill: Hydrodynamics and collision characteristics

R. Gers^{a,b}, E. Climent^{a,b}, D. Legendre^{a,b}, D. Anne-Archard^{a,b}, C. Frances^{c,d,*}

^a Université de Toulouse, INPT, UPS, IMFT (Institut de Mécanique des Fluides de Toulouse), Allée Camille Soula, F-31400 Toulouse, France

^b CNRS, IMFT, F-31400 Toulouse, France

^c Université de Toulouse, INPT, UPS, LGC (Laboratoire de Génie Chimique), 4, Allée Emile Monso, BP 84234, F-31432 Toulouse Cedex 4, France

^d CNRS, LGC, F-31432 Toulouse, France

A B S T R A C T

Producing nanoparticles in dense suspensions can be achieved in a stirred media mill. However the mechanisms of fragmentation in the mill are still not fully understood and the process remains laborious because of the large amount of supplied energy. We focus on the numerical analysis of the local hydrodynamics in the mill. Based on the flow simulations we determine the parameters which control the efficiency of the collisions between grinding beads (impact velocities and orientation of the collisions). The suspension flow (grinding beads, particles, carrying fluid) is modelled with effective physical properties. We solve directly the continuity and Navier–Stokes equations for the equivalent fluid assuming that the flow is two-dimensional and steady. Depending on the Reynolds number and the non-Newtonian behaviour of the fluid, we found that the flow is composed of several toroidal vortices. The most energetic collisions are driven by the strong shear experienced by the suspension within the gap between the disc tip and the wall chamber.

Keywords:

Simulation

Hydrodynamics

Particle processing

Wet milling

Suspension

Non-Newtonian fluids

1. Introduction

The need of nanoparticles has raised during the past few years. They enhance for example lifetime of paints, strength of materials, efficiency of pharmaceuticals or lubricants. Stirred media mills have proved to be an efficient way to produce nanoparticles, especially for poorly water soluble compounds (Mende et al., 2003; Merisko-Liversidge et al., 2003). Practically, the product must have a long residence time within the grinding chamber or be processed through several passes in a circulating mode in order to produce nanosize fragments. Many experiments have revealed that the particle size achieves a steady distribution during the fragmentation process. More particularly the mechanism of size reduction is not well understood and thus the limit fineness or the minimum achievable size is not well predicted. Limitations of the process may be of three types: mechanical, physicochemical or hydrodynamical. Depending on the material strength and structure, Bernotat and Schönert (1988) showed that the theoretical limit fineness related to the length of the fracture zone may vary from (1–10 nm) for brittle minerals to (1–10 μm) for plastics. In practice, such a minimum size is difficult to reach without the use of grinding aids or choosing optimum physicochemical conditions able to prevent screen attractive interparticle interactions

(Bernhardt et al., 1999; Mende et al., 2003; Garcia et al., 2004; Stenger et al., 2005a). Thus, physicochemical limitations raise because of the emergence of fragments below 1 μm inducing interparticle forces leading to the aggregation of fine particles. The third possible limitation is due to the process itself. Indeed when grinding beads collide, the squeezed fluid between the two surfaces of contact slows down their approaching motion due to lubrication. The dynamics of the fluid drainage depends on the fluid viscosity and the impact parameters. Therefore most of the available energy of the impact is dissipated in the fluid. Also, the fluid, which flows out of the gap, transports the particles away. Only particles remaining in this active volume may be crushed. Experiments have shown that the particle size, the solid concentration of the suspension and the physicochemical interactions between particle surfaces have a great influence during the size reduction process. However the role of each of these parameters regarding the impact velocity and the diameter of the grinding beads is unknown.

This study focuses on the hydrodynamics inside the grinding chamber. Its main purpose is to estimate collision velocities between grinding beads, as a function of the operating milling conditions (stirrer speed, flow rate, rheological properties of the suspension), without modelling contacts between grinding beads. Indeed, it is difficult to model accurately the contacts between grinding beads embedded in a suspension. That is why there are few Discrete Element Method (DEM) studies on wet grinding (Gudin et al., 2007; Mori et al., 2004). Yang et al. (2006) proposed a

* Corresponding author. Tel.: +33 534615252; fax: +33 534615253.
E-mail address: christine.frances@ensiacet.fr (C. Frances).

comparison of experimental measurements with DEM. In this approach the milling beads are followed in a Lagrangian framework. The beads experience successive collisions while the effect of the fluid is simply accounted for by a coefficient of viscous dissipation. Relating the numerical parameters of DEM simulations with the physical properties of the beads, the particles and the carrying fluid is a key issue of those models. Only very recently (Jayasundara et al., 2009), more advanced model include the simultaneous simulation of the bead trajectories supplemented by solving the fluid flow equation. These simulations are much more time consuming and required a careful modelling of the fluid-particle interactions. An alternative and very attractive approach for the prediction of the hydrodynamics is based on fluid flow studies and have been done for Newtonian fluids. For example, Blecher et al. (1996) have simulated the flow in the mill and the trajectories of isolated particles whose diameter varied from 250 μm to 1 mm. They concluded that beads may follow or not the flow according to a Motion Index which represents the ratio of the centrifugal force on the experienced drag force by the beads. Instead of a two-phase flow model, Lane (1999) preferred a simple approach based on the simulation of an equivalent fluid with the constant viscosity 1 Pa.s. As an indicator, he chose the viscous energy dissipation rate to estimate the local intensity of grinding.

The present paper investigates numerically the hydrodynamics within the mill, simulating the suspension flow by direct numerical solution of the continuity and Navier–Stokes equations for an equivalent fluid, accounting for the presence of both the grinding beads and the particles to be milled. The effective viscosity is modelled by a Krieger–Dougherty law where the viscosity depends on the particulate concentration. Since most of dense suspensions exhibit a non-Newtonian behaviour, results of simulations with shear-thinning or shear-thickening fluids are also discussed. Finally, collision velocities are estimated from the flow fields for frontal collisions and collisions induced by shear stress. Then, the available energy to break particles can be quantified according to the suspension properties.

2. Modelling approach

2.1. Mill design

Fig. 1 shows the design of an industrial stirred bead mill. For example, a similar mill was used in the experimental studies

presented in Garcia et al. (2004) or Frances and Anne-Archard (2004). In this type of mill (Fig. 1), the apparent volume of grinding is approximately filled up to 80% with monosized millimetric beads (from 100 μm to few mm diameter). This corresponds to an actual grinding media fraction of 50.4% according to a random close packing of 63% for the beads. The remaining of the volume contains a suspension of particles to be ground. The carrying fluid is often an aqueous solution with grinding aids. The beads and the suspension are strongly stirred by a central rotating agitator typically at a speed ranging from 1000 to 6000 rpm. The particle fragmentation results from the capture of particles inside zones of occurring strong stress when two grinding beads collide (frontal collisions in straining regions or oblique collisions induced by a local shear). The stirrer is usually composed of four perforated discs mounted on a driven shaft. The suspension flows continuously into the chamber. A rotating gap at the exit of the mill, used as a separation device, forces the grinding beads to stay inside the mill. A double jacket, where cooling water flows, allows the control of the temperature increase due to the size reduction process. However, in order to compare the results of our simulations with those previously obtained by Blecher et al. (1996) the geometrical dimensions of the mill reported in Table 1 were used. As a first step, the influence of holes in the discs has been neglected and discs are fully filled in our simulations. The presence of holes in the discs would affect moderately the flow field (assuming that the symmetry related to the disc plane still exists). The holes are likely to produce local changes in the velocity field but such effect is expected to be moderate in the absence of axial flow rate. When an axial flow is superimposed, axial velocity is present across the holes. Considering a typical value of 1.7 l/min, the mean axial velocity is about 5 mm/s in the gap corresponding to some percent of the disc tip speed V_θ showing that the expected 3D

Table 1

Actual dimensions of the mill and non-dimensional length scales (ΔR being the gap between the disc tip and the chamber wall).

Shaft radius R_s	21 mm	1.4 ΔR
Disc radius R_d	60 mm	4 ΔR
Inner chamber radius R_c	75 mm	5 ΔR
Gap between discs D_d	43 mm	2.8 ΔR
Disc thickness T_d	9 mm	0.6 ΔR
Chamber length L_c	380 mm	25.3 ΔR

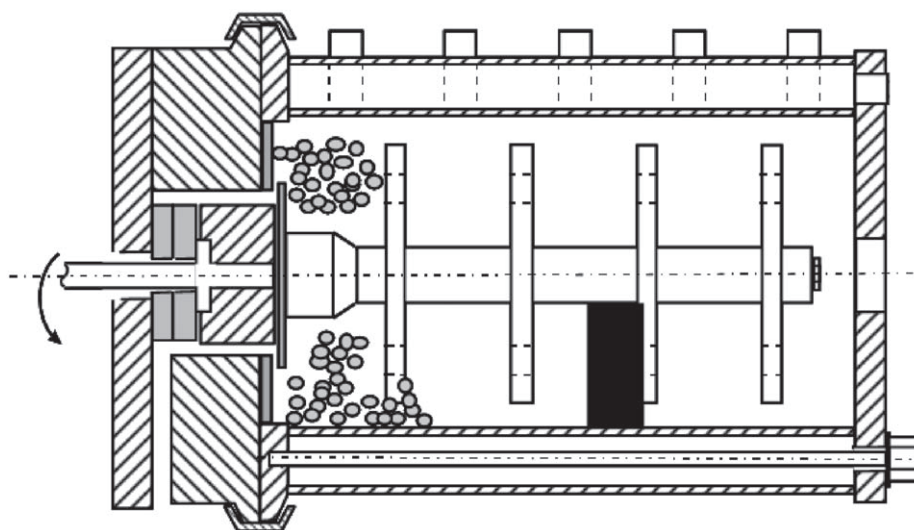


Fig. 1. Sketch of an industrial stirred media mill.

effect is presumably of minor importance. The most important length scales are the shaft radius, the disc radius and the inner chamber radius because they determine the flow in the mill.

2.2. Numerical method

The computations reported in this paper have been carried out with the numerical code JADIM presented in details in numerous references (Magnaudet et al., 1995; Legendre and Magnaudet, 1998; Legendre et al., 2003). Its ability to simulate cylindrical Couette flows has been recently presented in Climent et al. (2007). The code JADIM solves the continuity and the three-dimensional unsteady Navier–Stokes equations written in velocity–pressure variables in a general system of orthogonal curvilinear coordinates. For the present problem, these equations are:

$$\nabla \cdot \mathbf{v} = 0 \quad (1)$$

$$\rho_{eff} \left(\frac{\partial \mathbf{v}}{\partial t} + \mathbf{v} \cdot \nabla \mathbf{v} \right) = -\nabla p + \nabla \cdot (\mu_{eff} (\nabla \mathbf{v} + \nabla^t \mathbf{v})) \quad (2)$$

where ρ_{eff} is the effective fluid density, \mathbf{v} the fluid velocity, p the pressure, μ_{eff} the effective fluid viscosity. We introduce the disc tip speed as $V_\theta = v_\theta(r = R_d)$. The spatial discretization is based on a staggered mesh and the equations are integrated in space using a finite volume method with second-order accuracy, all spatial derivatives being approximated using second-order schemes. The temporal evolution is achieved through a Runge-Kutta-Crank-Nicholson algorithm, which is second-order accurate in time. Finally, incompressibility is satisfied at the end of each time step by solving a Poisson equation for an auxiliary potential. The axisymmetric grid is Cartesian and is made of 118×62 grid points along the radial and axial directions, respectively. We have done some preliminary tests to verify that the results are independent of the number of nodes used to discretize the domain.

Accounting for symmetries in the mill, the flow can be simulated in the plane represented in Fig. 2 in axisymmetric framework of reference: r is the radial coordinate, z the axial coordinate and θ the tangential coordinate. In actual operations, the mill is horizontal. But, gravity has no effect in our simulations while the equivalent fluid is assumed to be homogeneous. The gap between the disc tip and the chamber wall is called ΔR and is selected to scale all the length scales of the geometry. This simulation domain illustrated in Fig. 2 is bounded by the mill wall on the right ($r/\Delta R = 5$), the shaft wall on the left ($r/\Delta R = 1.4$) and two planes of symmetry (on the top $z/\Delta R = 1.73$, at the bottom $z/\Delta R = 0$). The grid is refined near the wall in order to capture the velocity gradients for the largest considered Reynolds number. Typically, the grid spacing is $8.7 \times 10^{-3} < \Delta z/\Delta R < 4 \times 10^{-2}$ and $9.3 \times 10^{-3} < \Delta r/\Delta R < 3.9 \times 10^{-2}$ along the radial and axial directions, respectively. Distinct boundary conditions are applied on the frontiers of the computational domain: no-slip conditions are imposed on the walls and symmetry conditions are imposed on the others boundaries. The wall condition consists in imposing the velocity of rotation of the inner wall while zero velocity is imposed on the outer non-rotating cylinder. A tangential velocity was imposed on the stirrer wall to reproduce the rotation motion. Typically, a rotation frequency of 955 rpm corresponds to disc tip speed $V_\theta = 6$ m/s. The hydrodynamics within the mill has been simulated in a dimensionless form and the tip speed of 6 m/s is only given as a possible reference to a practical case. The same value of the Reynolds numbers may be achieved with doubling the tip speed and the viscosity. Higher viscosity in the mill are likely to occur during the process (size reduction enhances adhesion forces) or with operating conditions corresponding to larger mass loading of the particle suspension. Simulations are initialized by a composite solution based on a solid body rotation ($r \leq R_d$) and a pure Couette flow ($r \geq R_d$). We are only interested in the steady flow patterns as milling operations are generally operated out over long times. To study distinct Reynolds number configurations, the fluid viscosity is

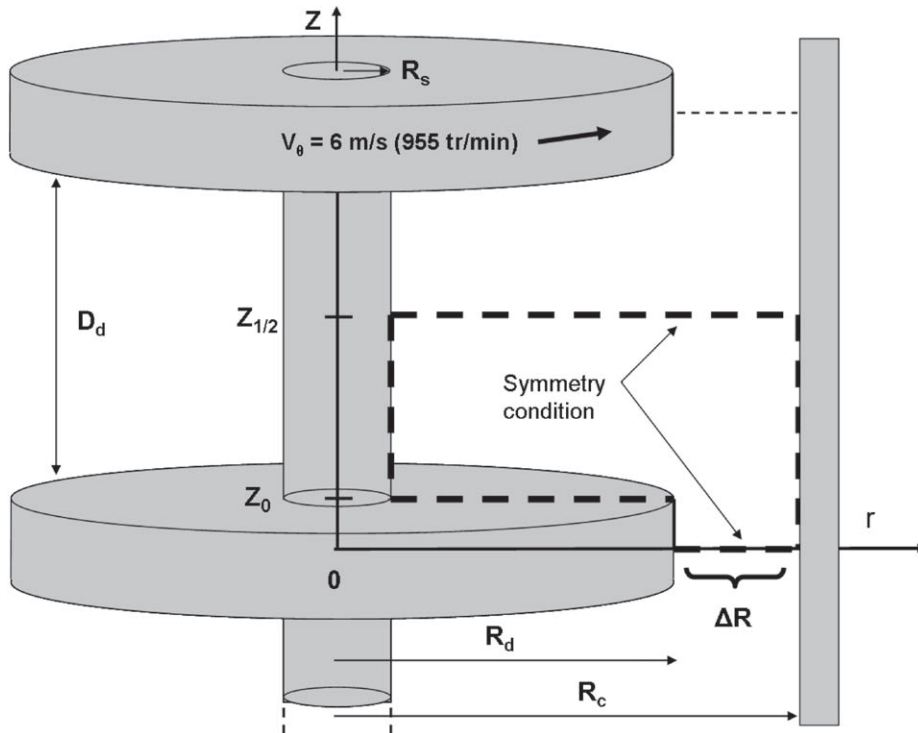


Fig. 2. Sketch of the simulation domain and its boundary conditions.

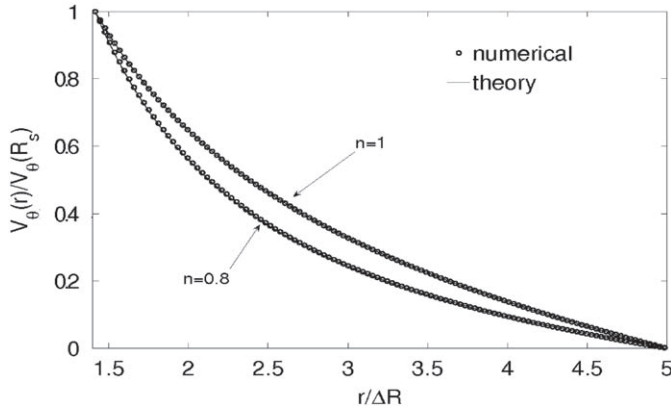


Fig. 3. Radial profile of the tangential velocity in a cylindrical Couette flow for Newtonian and non-Newtonian fluids at $Re = 73$ ($n = 1$ and $n = 0.8$). Solid line: analytical solution (Eq. 3); \bullet : numerical simulations.

gradually decreased. For a given viscosity, the simulation is initialized by a previous solution and the flow evolves during a transient time before converging to a new steady state. In view of this study, additional tests have been performed. Two basic flows of non-Newtonian fluids have been computed for conditions closed to the present study: a non-Newtonian Poiseuille flow and a non-Newtonian Couette flow. For the Poiseuille flow the numerical results were compared to the exact analytic solution and a very good agreement was achieved for both Newtonian and non-Newtonian fluids. The maximum relative errors $(u_{numerical} - u_{analytical})/u_{max}$ are 5.5×10^{-4} and 0.002, respectively. Similar tests have been performed for the Couette Flow. The radial profile of the azimuthal velocity v_θ is reported in Fig. 3 for a Newtonian fluid and for a non-Newtonian fluid ($m = 0.1$ and $n = 0.8$). See definitions of m and n in the next section. The simulations have been carried out under conditions similar to the ones which were used for the mill simulations. The dimension of the outer non-rotating cylinder is defined by $R_c/\Delta R = 5$ (radius 75 mm) while the inner rotating cylinder radius is $R_s/\Delta R = 1.4$ (radius 21 mm). Here $\Delta R = R_c - R_s$ is the gap between the two cylinders. The Reynolds number based on the inner cylinder diameter is $Re = 73$ corresponding to the rotation frequency ω of 100 rad s^{-1} or 15.9 rounds per second. At this moderate Reynolds number no instability of flow is expected. The numerical simulations are compared with the analytic velocity profile:

$$v_\theta(r) = \omega \frac{R_s^{2/n}}{R_s^{2/n} - R_c^{2/n}} r \left(1 - \left(\frac{R_c}{r} \right)^{2/n} \right) \quad (3)$$

where n is the fluid index defined by Eq. (6). A very good agreement is again achieved between the numerical simulations and the Eq. (3) as shown by Fig. 3. The maximum relative errors $(v_\theta^{numerical} - v_\theta^{analytical})/V_\theta$ are 4×10^{-5} and 0.02 for Newtonian and non-Newtonian fluids, respectively.

2.3. Suspension modelling

The actual flowing phase in a stirred media mill is complex because it is a polydisperse suspension composed of the carrying fluid, the particles to be crushed and the grinding beads. The fluid phase carries grinding beads but a strong dissipation of energy occurs through lubrication effects during bead collision and particle breakage. Feed particles become smaller and smaller and modify the suspension viscosity which controls the collision intensities between beads. Nevertheless the size ratio between grinding beads and particles is always high. It ranges from 10 or

more to roughly 1000. The particle suspension can therefore be considered as a homogeneous media for the grinding beads.

Another quantity of interest to characterize the flowing phase is the mean distance between grinding beads δ . It is estimated by the relation (Shook and Rocco, 1991):

$$\delta = \left[\left(\frac{\phi_m}{\phi} \right)^{1/3} - 1 \right] d_{GM} \quad (4)$$

where ϕ and ϕ_m are, respectively, the volume fraction and the random close packing fraction (63%) and d_{GM} is the diameter of the grinding beads. For the usual volume fraction $\phi = 50.4\%$, this leads to $\delta/d_{GM} \sim 8\%$. δ can be regarded as half the free average spacing for a grinding bead. No experimental evidences are currently available about the spatial grinding media distribution in the mill. Nevertheless this low value of δ is not likely to induce strong inhomogeneities.

Consequently, we assume that the dispersed phase composed of the grinding beads and the particles are uniformly distributed throughout the mill. This means that the centrifugal segregation due the fluid rotation is neglected. Such effect may occur for suspensions of heavy particles. However, the volume fraction of the solid phase (beads and particles) is very high (80%) and significant variations of the solid fraction are only expected close to the shaft where the collision intensity is weak (see the following results). Our assumption concerning the radial segregation is confirmed by the recent simulations coupling the DEM approach for the beads with the solution of the Navier–Stokes equations for the equivalent fluid (fluid+particles) performed by Jayasundara et al. (2009). Despite a lower volume fraction for the solid phase (70%), this study showed a significant reduction of centrifugal segregation when the fluid viscosity is increased. For the viscosity range considered in our study, the segregation has almost disappeared. Concerning the particle motion inside the secondary flows, the discrepancy between the fluid streamlines and the bead trajectories can be characterized by a Stokes number $St = \tau_{GM}/\tau_f$ where τ_{GM} is the viscous relaxation time of a bead ($\tau_{GM} = (1/18)(\rho_{GM} + \rho_{sup}/2)d_{GM}^2/\mu_{sup}$) and τ_f a time scale of the fluid flow that can be estimated by $\Delta R/U$ (U is characteristic of the strength of secondary flows: 10–25% of the tangential velocity of the discs). St varies between 0.1 and 1 in the range of operating conditions investigated here. This moderate value of the Stokes number indicates that the beads are likely to follow the fluid streamlines in the secondary flows. So an equivalent one-fluid model can reasonably be used to avoid the complexity of a multiphase flow approach without losing the global specific characteristics of the fluid. Lane (1999) proposed similar numerical simulations for a viscosity of 1 Pa.s. In our simulations, the viscosity of the equivalent fluid is estimated from experimental data of particle suspension and using the Krieger–Dougherty model to evaluate the overall viscosity, including the effect of the grinding beads and particle suspension:

$$\mu_{eff} = \mu_{susp} \left(1 - \frac{\phi}{\phi_m} \right)^{-5/2\phi_m} \quad (5)$$

where μ_{susp} is the viscosity of the particle suspension considered as the carrying fluid for the grinding beads. Values of μ_{susp} can be extracted from a previous experimental study (Frances and Anne-Archard, 2004) in which the rheological behaviour of a ground suspension of calcium carbonate CaCO_3 (2700 kg/m^3) was characterized. For sufficient grinding aids concentration and for volumetric concentration varying 8–27% (mass fraction between 20% and 50% corresponding to a bulk density of the suspension ρ_{susp} varying from 1340 to 1850 kg/m^3), the behaviour reveals to be virtually Newtonian to slightly shear-thinning. Rheological properties change rapidly when the additives concentration is

decreasing and one can observe highly shear-thinning behaviour with low consistency index or even a viscoplastic behaviour. We restricted our study to usual behaviour encountered in grinding processes, that is to say with usual additives concentrations. While the size of the particles of the suspension is reducing due to the grinding process, a significant increase of the viscosity is more likely to occur (resulting in a decrease of the Reynolds number) supplemented by a non-Newtonian behaviour. This evolution occurs on time scales much longer than the time required to reach hydrodynamic steady conditions. Therefore our simulations correspond to different stages of the size reducing process. Considering the density of each material (particles and grinding media), the kinematic viscosity $\nu_{eff} = \mu_{eff} / \rho_{eff}$ ranges from 10^{-3} to $3.3 \times 10^{-4} \text{ m}^2/\text{s}$ which is consistent with experimental observations.

Shear-thinning behaviour observed in the experiments is fitted using a power-law model for the equivalent fluid:

$$\tau = m\dot{\gamma}^n \quad (6)$$

where τ and $\dot{\gamma}$ are, respectively, the shear stress and the shear rate, m the consistency and n the fluid index. $\dot{\gamma}$ is calculated from the components of the strain tensor S :

$$\dot{\gamma} = \sqrt{2 \text{tr}(S^2)} \quad (7)$$

where the strain tensor S is defined by:

$$S = 1/2(\nabla\mathbf{v} + \nabla^t\mathbf{v}) \quad (8)$$

As shear-thickening behaviour may also be observed in concentrated suspensions under high shear rate (Barnes et al., 1989), numerical simulations with values of n -index greater than 1 will be also be discussed.

2.4. Reynolds number definition

The flow regime is characterized by the Reynolds number. Depending on hydrodynamics features under interest, different Reynolds number definitions can be selected. The very widely used definition for mixing systems is based on the rotation frequency N and on the agitator diameter D (Nagata, 1975). In Newtonian cases, its expression is:

$$Re = \rho_{eff} \frac{ND^2}{\mu_{eff}} \quad (9)$$

where ρ_{eff} is the effective suspension density and μ_{eff} the effective suspension viscosity. Considering non-Newtonian fluids, a generalized Reynolds number is defined in order to account for the variations of the fluid viscosity through the fluid index n and the consistency index m :

$$Re_g = K_s^{1-n} \rho_{eff} \frac{N^{2-n} D^2}{m} \quad (10)$$

This extension of the Reynolds number is based on power consumption considerations using the broadly accepted Metzner-Otto concept (Chhabra, 2003). This postulates that the effective shear rate of the flow is proportional to the rotation frequency through a coefficient K_s . It was shown in the experiments that K_s is only a function of the impeller-vessel configuration, at least as long as the index behaviour n of the fluid is not too small. Although K_s values are proposed in literature for various mixing systems, there is no systematic study available for mills. So we use the analytic expression obtained for Taylor-Couette flow in concentric cylinders with a radius ratio s equal to R_d/R_c :

$$K_s = 4\pi n^{n/(1-n)} \left(\frac{(1-s^{2/n})^n}{1-s^2} \right)^{1/(1-n)} \quad (11)$$

3. Spatial structure of the flow field

We used direct numerical simulations of the continuity and Navier–Stokes equations to analyse the flow behaviour in the mill. Depending on the nature of surface interactions between particles and between the grinding beads, the suspension may behave as a Newtonian or a non-Newtonian fluid. We started to study the evolution of the flow patterns within the chamber for a Newtonian fluid as the reference case. As the Reynolds number is the only non-dimensional parameter governing the flow dynamics, the disc rotation rate or the viscosity may be equivalently varied for a fixed geometry. The rotation frequency has been maintained constant throughout the study, imposing a constant tangential velocity of the disc V_θ and we varied the viscosity of the suspension to study different Reynolds numbers. The effect of the overall non-Newtonian hydrodynamics has been investigated assuming a power law rheological behaviour (shear-thinning or shear-thickening). Velocity fields and contour levels of energy dissipation are presented in the visualization plane (r, z) . The correspondence of the numerical parameters with the physical operating conditions has been summarized in Table 2.

3.1. Hydrodynamics in the newtonian cases

3.1.1. Flow patterns

At very low Reynolds number, the flow is purely azimuthal. Beyond a critical value of the Reynolds number, secondary flows in the axial–radial plane (r, z) appear. Secondary flows in the (r, z) plane and viscous energy dissipation rate are presented in Figs. 4, 5 and 6 for Reynolds number equal to 229, 458 and 654, respectively. The fluid rotation between the disc tip and the fixed wall of the mill generates an instability driven by the centrifugal force. This configuration is strictly similar to the Couette-Taylor instability occurring in the gap between two cylinders (the inner cylinder is rotating while the outer one stays at rest). As the instability sets in, a single toroidal vortex develops in the mill (see the streamlines plotted in Fig. 4a).

Further increase of the Reynolds number modifies drastically the flow structure (Figs. 5a and 6a). Two contra-rotating vortices fill the whole mill chamber. One strong vortex is located in the gap between the rotating disc tip and the fixed outer cylinder. The largest vortex (less energetic) fills the remaining area of the simulated domain. When the Reynolds number increases from 458 to 654, the small vortex expands. The strength of these secondary flows is an increasing function of the Reynolds number. The maximum intensity of the flow in the (r, z) plane is ranging between 20% and 25% of the tangential velocity of the disc tip. It is well known that further increase of the Reynolds number in the Taylor–Couette apparatus leads to an unsteady behaviour of the vortices (azimuthal wavy oscillation) but we did not observe this transition in our configuration. This second transition of the flow is unlikely to occur in the context of stirred media milling because

Table 2
Characteristics of the fluids.

Fluid type	Rheological properties	Re
Newtonian	$\nu_{eff} = 1 \times 10^{-3} \text{ m}^2 \text{ s}^{-1}$	229
	$\nu_{eff} = 5 \times 10^{-4} \text{ m}^2 \text{ s}^{-1}$	458
	$\nu_{eff} = 3,5 \times 10^{-4} \text{ m}^2 \text{ s}^{-1}$	654
Shear-thinning	$m/\rho_{eff} = 1 \times 10^{-3} \text{ m}^2 \text{ s}^{n-2}$ and $n = 0.9$	422
	$m/\rho_{eff} = 5 \times 10^{-4} \text{ m}^2 \text{ s}^{n-2}$ and $n = 0.9$	845
Shear-thickening	$m/\rho_{eff} = 3,5 \times 10^{-4} \text{ m}^2 \text{ s}^{n-2}$ and $n = 1.2$	67

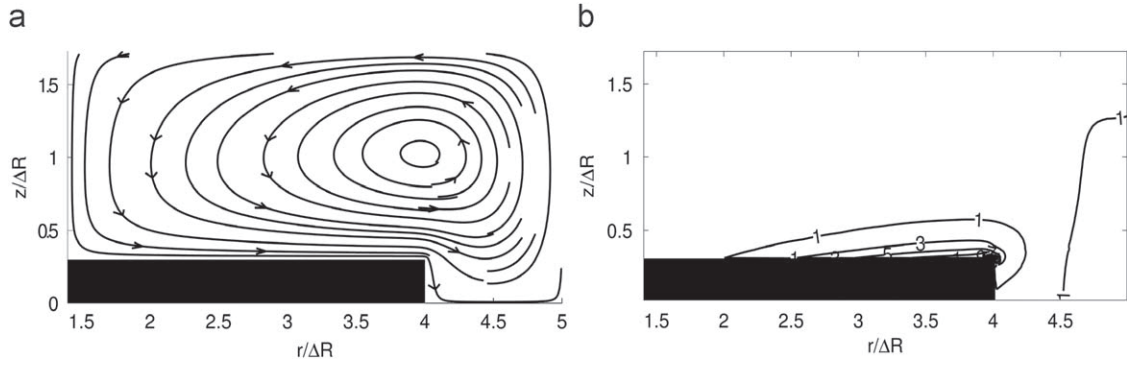


Fig. 4. Streamlines on the left (a) and contour levels of the non-dimensional viscous energy dissipation rate on the right (b) for a Newtonian fluid, $Re = 229$.

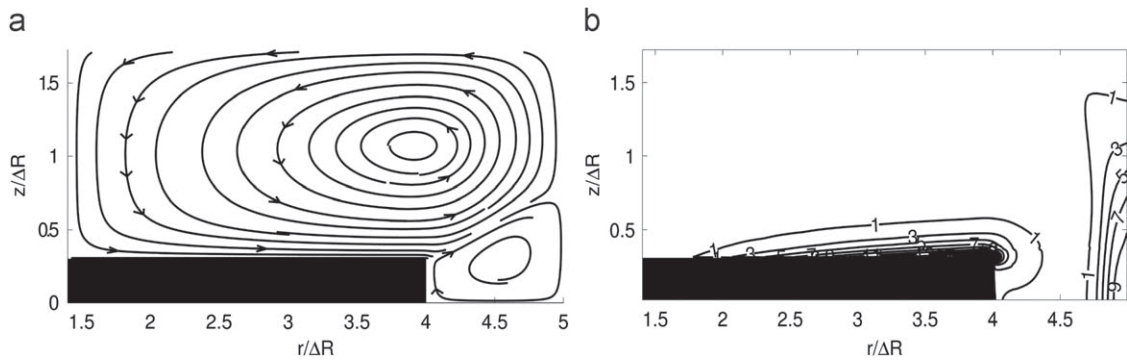


Fig. 5. Streamlines on the left (a) and contour levels of the non-dimensional viscous energy dissipation rate on the right (b) for a Newtonian fluid, $Re = 458$.

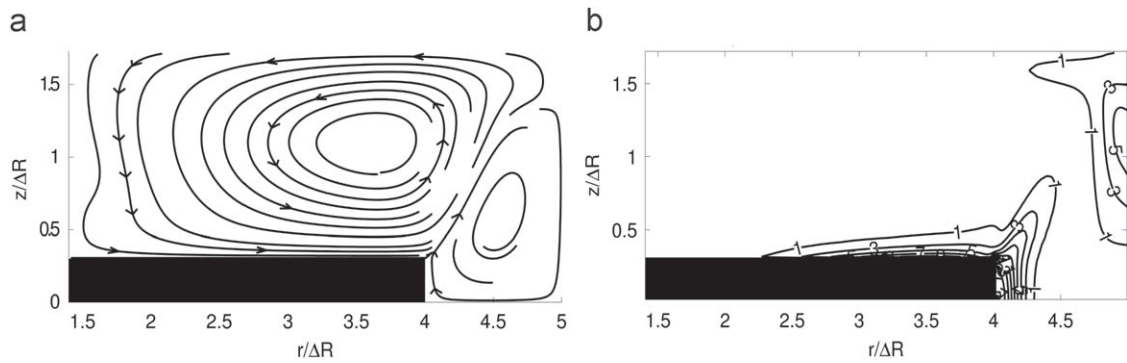


Fig. 6. Streamlines on the left (a) and contour levels of the non-dimensional viscous energy dissipation rate on the right (b) for a Newtonian fluid, $Re = 654$.

the effective suspension viscosity is generally high and limits the Reynolds number to moderate values.

Similar stationary toroidal vortices have been already observed by several authors. Theuerkauf and Schwedes (1999) presented a comparison between simulations and experiments where the presence of secondary flows was clearly identified. These challenging measurements were made possible by using an equivalent transparent fluid. The numerical study of the turbulent flow was done by means of a $k-\varepsilon$ model. Their results were extended to a Reynolds number of 16000 in Theuerkauf and Schwedes (2000). But in all their results, a single vortex was observed in the (r, z) plane. Among papers devoted to the study of the hydrodynamics in the mill, only the study of Lane (1999) (simulations with open holes in the discs) has revealed the presence of several vortices as we observe for Reynolds numbers 458 and 654 (Figs. 5a and 6a). As mentioned by Theuerkauf and Schwedes (1999), the flow is controlled by the fluid behaviour between two discs. The mill geometries which slightly differ

($\Delta R/R_c = 0.33$ and $D_d/R_c = 0.8$ in their case) may explain the discrepancies between both results. Nevertheless, they found only one vortex in their simulations whatever the Reynolds number. This is more likely due to the high effective viscosity induced by the $k-\varepsilon$ model. The effective viscosity in a Reynolds averaged model corresponds to the contributions of the molecular viscosity (around $4.8 \times 10^{-4} \text{ m}^2 \text{ s}^{-1}$ in their case) and the turbulent viscosity (probably one or two orders of magnitude larger than the physical viscosity). As a consequence their flow pattern for a Reynolds number of 16000 is similar to the flow pattern we obtained for a Reynolds number of 229.

Although the secondary toroidal flows are not very energetic, they play a major role in the grinding process. If the flow was purely azimuthal whatever the Reynolds number, the motion of the suspension would remain on closed pathlines around the shaft. The secondary flows force the suspension to follow complex trajectories all the way through the entire volume of the grinding chamber as mentioned by Blecher et al. (1996). The milling

efficiency is enhanced by applying a net axial flow through the mill. It is known that the axial flow rate decreases the mean residence time of particles in the mill according to Weller et al. (2000). Simulations were carried out to study the effects of a mean axial flow on the hydrodynamics. For that purpose the flow rate was varied from 0 to 100 l/h (1.7 l/min) which is a typical operating condition for laboratory stirred media mills. Those simulations were performed out with a refined mesh and by imposing periodic boundary conditions between $z = z_{1/2}$ and $z = -z_{1/2}$ supplemented by an appropriate mean pressure gradient in the axial direction (see Fig. 2). No noticeable modification of the flow structure and velocity profiles were observed. It can be explained by the very low mean axial velocity even in the smallest sections of the mill corresponding to the gap between the disc tip and the chamber wall. The mean axial velocity corresponding to 100 l/h is less than 0.1% of V_θ . Therefore, only results with zero axial flow will be discussed in the remaining of the paper. The enhanced efficiency observed experimentally with this axial mean flow is probably related to the mixing of the suspension, especially close to the exit of the mill.

In Fig. 7, we compare the radial profiles of the non-dimensional tangential velocity v_θ/V_θ in the vicinity of the disc ($z = z_0$) and along the symmetry plane between two discs ($z = z_{1/2}$), see the sketch in Fig. 2 for the definition of z_0 and $z_{1/2}$. The slope of the velocity distribution is modified when the ratio between inertia and viscous effects is increasing. Steep gradients of velocity are expected in the regions close to rotating walls as the boundary layer is becoming thinner. This effect is particularly obvious within the gap between the disc $r/\Delta R = 4$ and the fixed wall $r/\Delta R = 5$. When the Reynolds number increases from 229 to 654, the shape of the profile is conserved but the radial gradient of the tangential velocity is steeper in the vicinity of the disc whatever the plane. In the plane $z = z_{1/2}$ when the Reynolds number is increased from $Re = 458$ to $Re = 654$, we observe the progressive motion of the fluid between the discs toward a region experiencing a solid body rotation flow close to the shaft (between $r/\Delta R = 1.4$ and $r/\Delta R = 2$). From $r/\Delta R = 2$ to $r/\Delta R = 4$ the tangential velocity is approximately constant but higher for $Re = 654$ than for $Re = 458$ and decreases toward zero on the fixed wall ($r/\Delta R = 5$). Based on these observations, it is obvious that the radial gradient of the tangential velocity in the gap between the disc tip and the fixed chamber wall is very strong and is likely to be the dominant contribution to the viscous energy dissipation.

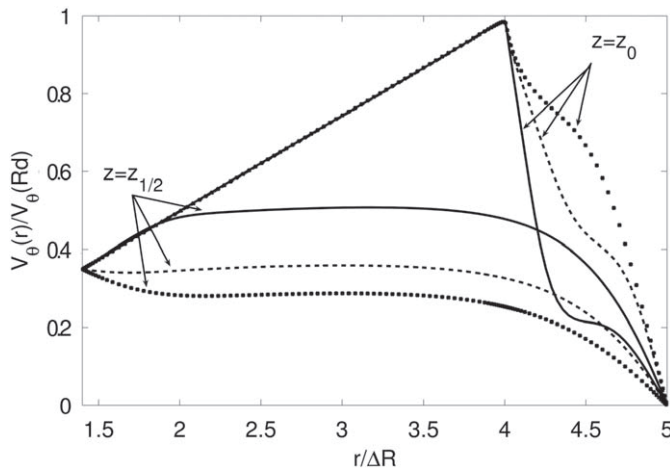


Fig. 7. Radial profile of the tangential velocity at the surface of the disc ($z = z_0$) and at the symmetry axis between two discs ($z = z_{1/2}$) for $Re = 654$ (continuous line), $Re = 458$ (dashed line) and $Re = 229$ (dotted line).

3.1.2. Spatial distribution of the energy dissipation

The local rate of energy dissipation by viscous friction is a spatial indicator of the comminution efficiency (Blecher and Schwedes, 1996). Energy supplied to the stirrer is dissipated in regions of high shear forcing to collisions between grinding beads and particles. In these regions of the flow, collisions are expected to be very energetic and consequently the comminution to be the most efficient. In cylindrical coordinates the energy dissipation rate $P = 2\mu(S : S)$ is written as follows:

$$\frac{P}{\mu_{eff}} = 2 \left(\frac{\partial v_r}{\partial r} \right)^2 + 2 \left(\frac{v_r}{r} \right)^2 + 2 \left(\frac{\partial v_z}{\partial z} \right)^2 + \left(\frac{\partial v_\theta}{\partial r} - \frac{v_\theta}{r} \right)^2 + \left(\frac{\partial v_z}{\partial r} + \frac{\partial v_r}{\partial z} \right)^2 + \left(\frac{\partial v_\theta}{\partial z} \right)^2 \quad (12)$$

In a pure shear flow, P is related to the shear rate by the relation $P = \mu_{eff} \dot{\gamma}^2$. Note that for generalized Newtonian fluids (see definition in Eq. (6)) Eq. (12) is still valid as long as the viscosity μ_{eff} is evaluated from the local shear rate. The energy dissipation rate is scaled by $P_{ref} = \mu_{eff} \dot{\gamma}_{ref}^2$ where $\dot{\gamma}_{ref} = V_\theta/\Delta R$ and we define $P^* = P/P_{ref}$. The Figs. 4b, 5b and 6b show the contours of P^* while the Reynolds number is increased. For the lower Reynolds number, the region of high dissipation rate is confined close to the disc where the gradient of the tangential velocity in the z -direction ($\partial v_\theta/\partial z$) dominates the other components of the strain rate tensor. When the Reynolds number is increased, the enhancement of the second toroidal vortex is accompanied by a strong gradient in the r -direction ($\partial v_\theta/\partial r$) between the disc and the fixed outer wall of the mill. This contribution becomes dominant by $Re = 654$. In Figs. 4b, 5b and 6b isolines of P^* are closely related to contour levels of the shear rate. Typically, for the Newtonian fluids considered in our study, a shear rate of 1000 s^{-1} corresponds to a $P^* = 6.25$. High energy dissipation rates (corresponding to $P^* > 1$) occur in two narrow areas: near the disc surface and along the chamber wall. Both regions become thinner as the Reynolds number increases. This contraction of high energy dissipation areas was first highlighted by Blecher et al. (1996). Together with this reduction of areas, the maximum of viscous energy dissipation strongly increases between $Re = 229$ and $Re = 458$ ($P^*_{max} = 35$ for $Re = 229$ and $P^*_{max} = 80$ for $Re = 458$), but decreases at $Re = 654$ ($P^*_{max} = 28$). Finally, we observe that the area close to the chamber wall moves toward the symmetry axis while the area near the disc moves toward the disc tip. This has to be related to the modification of the flow structure with increasing Re .

3.2. Hydrodynamics of non-Newtonian fluids

During the grinding process, comminution of feed particles may lead to dramatic modifications of the suspension. If a size reduction occurs, surface interactions between particles or between particles and beads will strongly evolve. Fluid behaviour becomes more and more shear-thinning, and as volume fractions are high, shear-thickening behaviour may also appear. Then it was of particular interest to analyse effects of such non-Newtonian characteristics. The consistency m and the fluid index n characterize the non-Newtonian behaviour of the fluid (cf. Eq. (6)). When $n < 1$ the fluid has a shear-thinning behaviour and the effective viscosity $\mu_{eff} = m \dot{\gamma}^{n-1}$ is a decreasing function of the shear rate. If $n > 1$ the fluid will be shear-thickening.

3.2.1. Shear-thinning fluid

We selected the value $n = 0.9$ and varied the pseudo-consistency from $m/\rho_{eff} = 1 \times 10^{-3} \text{ m}^2 \text{ s}^{n-2}$ to $m/\rho_{eff} = 5 \times 10^{-4} \text{ m}^2 \text{ s}^{n-2}$ corresponding to the Figs. 8 and 9 where the generalized Reynolds number is, respectively, equal to 422 and 845.

Even though the fluid index has been slightly varied from the Newtonian behaviour, the flow patterns are significantly modified

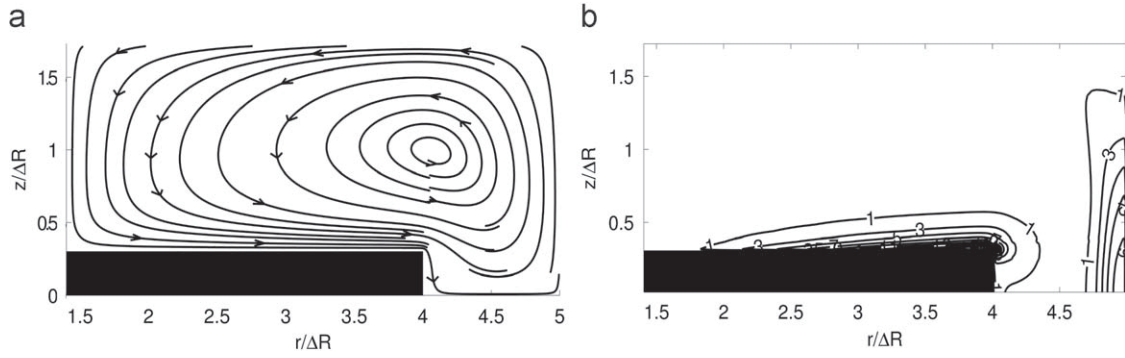


Fig. 8. Streamlines on the left (a) and contour levels of the non-dimensional viscous energy dissipation rate on the right (b) for a shear-thinning fluid, $Re = 422$.

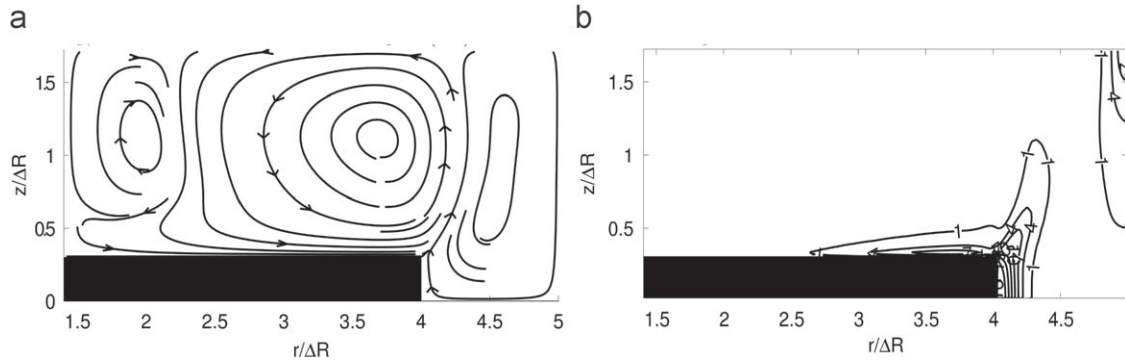


Fig. 9. Streamlines on the left (a) and contour levels of the non-dimensional viscous energy dissipation rate on the right (b) for a shear-thinning fluid, $Re = 845$.

especially the secondary flows. Indeed, the configuration corresponding to $Re = 422$ leading to streamlines in Fig. 8 is similar to the Newtonian flow pattern observed for $v_{eff} = 1 \times 10^{-3} \text{ m}^2 \text{ s}^{-1}$. The strength of the secondary flow ranges within the same order of the magnitude (20–25% of the maximum azimuthal velocity). But, the simulations corresponding to $m/\rho_{eff} = 5 \times 10^{-4} \text{ m}^2 \text{ s}^{n-2}$ and $n = 0.9$ lead to the formation of a third vortex in the (r, z) plane. This new vortex has a very low rotation intensity typically less than 2% of the reference velocity scale. This evolution may be related to an increase of the generalized Reynolds number. The local reduction of the effective viscosity in regions of high shear rate induces a centrifugal forcing. As inertia is gradually increased, secondary flows are able to develop.

As shown in Figs. 4b and 8b, the areas of high viscous dissipation rate (from $P^* = 1$ to its maximum value) have shrunk when the Newtonian fluid of effective viscosity $v_{eff} = 1 \times 10^{-3} \text{ m}^2 \text{ s}^{-1}$ has been substituted by a shear-thinning fluid ($m/\rho_{eff} = 1 \times 10^{-3} \text{ m}^2 \text{ s}^{n-2}$ and $n = 0.9$). In the same time, P_{max}^* has increased: for $Re = 422$, $P_{max}^* = 56$ instead of 35 for the Newtonian case. Thus, the areas of high energy dissipation are more spread. Similarly, areas of high viscous dissipation rate have shrunk when the Newtonian fluid of effective viscosity $v_{eff} = 5 \times 10^{-4} \text{ m}^2 \text{ s}^{-1}$ has been substituted by a shear-thinning fluid described by $m/\rho_{eff} = 5 \times 10^{-4} \text{ m}^2 \text{ s}^{n-2}$ and $n = 0.9$. But in this case, P_{max}^* decreases ($P_{max}^* = 22$ instead of 80 for the corresponding Newtonian case).

Again, we tested the influence of a net axial flow rate of 85 L/h on the structure and intensity of secondary flows and maximal viscous dissipation rate contours. We found that the modifications were only minor.

3.2.2. Shear-thickening fluid

This behaviour is encountered in very high concentrated suspensions experiencing high shear rates (Barnes, 1989). The

results of the simulation (Fig. 10) with a shear-thickening fluid (consistency $m/\rho_{eff} = 1 \times 10^{-3} \text{ m}^2 \text{ s}^{n-2}$ and $n = 1.2$) are compared to the Newtonian behaviour corresponding to a viscosity $v_{eff} = 1 \times 10^{-3}$ (Fig. 4). The shape of the streamlines are almost similar but the maximum velocity in the (r, z) plane is twice lower. Again, this can be interpreted in terms of the reduction of the generalized Reynolds number (67 for the shear-thickening fluid and 229 for the Newtonian fluid). Consequently, the regions of high shear rate are drastically reduced to a small area along the disc tip. Any influence of the flow rate is noticeable.

4. Determination of collision characteristics

Based on simulations of the global dynamics of the effective fluid in the mill chamber, we propose an analysis of the local flow experienced by grinding beads. We aim at providing a quantitative prediction of collisions intensity of the beads which is the energy available for comminution of the feed particles. Indeed, the purpose of this section is to estimate the kinetic energy, the geometric configuration and the range of non-dimensional parameters characterizing the impact of two neighbouring beads embedded in the suspension.

4.1. Different types of collision

The comminution of the feed particles in a stirred media mill may be inferred to two distinct mechanical phenomena. The particles are either squeezed between two colliding grinding beads or between a bead and a wall. Centrifugal force of the suspension is related to the tangential mean flow induced by the high speed rotating shaft and discs. Particles and beads in the vicinity of the outer wall of the mill chamber ($r/\Delta R = 5$) are experiencing a high pressure. This contribution to the process can

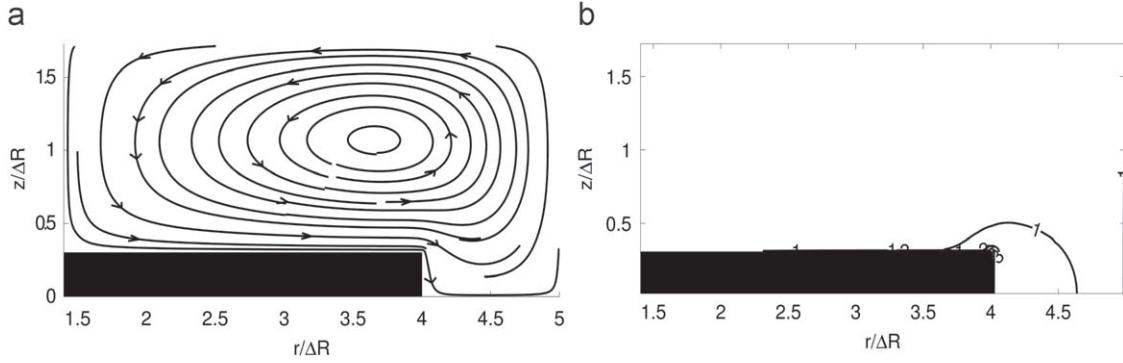


Fig. 10. Streamlines on the left (a) and contour levels of the viscous energy dissipation rate on the right (b) for a shear-thickening fluid, $Re = 67$.

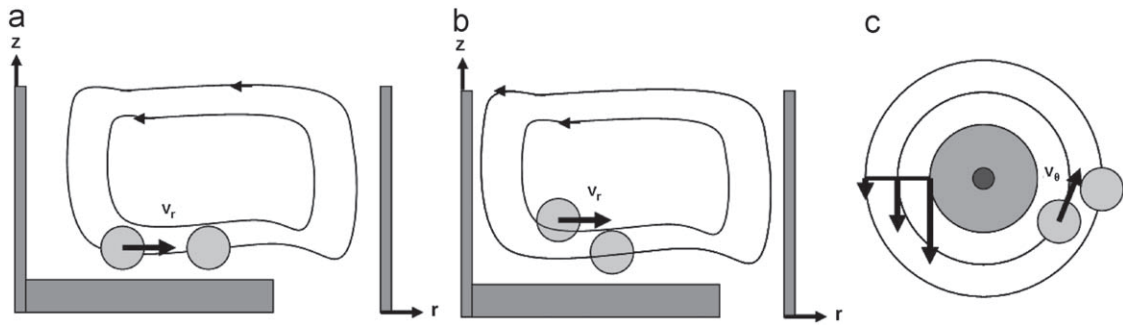


Fig. 11. Sketches of a frontal collision between two beads following the same streamline (a), an oblique collision between two beads following different streamlines in the (r, z) plane (b) and an oblique collision between two beads having circular trajectories in the (r, θ) plane (c).

be evaluated by analysing the magnitude of the pressure at the wall for the equivalent fluid. However, Kwade (1999) found that this particular mechanism was not dominant. So we will consider only the second mechanism which is induced by bead-bead collisions. Two types of collision between grinding beads can be distinguished. The first configuration of impact is called frontal collision: the relative velocity of the beads and the beads centre line are aligned. This configuration is encountered when the beads are moving along the same streamline but with different velocities (Fig. 11a). In all the other cases, collisions can be called oblique collisions because induced by local shearing of the flow. The beads are moving along distinct parallel streamlines (Fig. 11b and c). In the (r, z) plane, the presence of secondary flows is forcing oblique and frontal collisions. The intensity and the orientation of the impact are related to the local flow properties. These collisions may occur simultaneously within the mill in the (r, z) plane and in the (r, θ) plane. Due to the fluid rotation in the azimuthal direction only oblique collisions are expected in the (r, θ) plane (Fig. 11c).

4.2. Impact parameters

For determining the physical characteristics of beads impact within the mill, we need to estimate the relative velocity when the contact occurs. Based on the simulations of the effective fluid flow which models the overall dynamics of the suspension, the prediction of collision properties is related to the rate of deformation of the fluid flow. Indeed, any flow field can be split into two distinct contributions: strain deformation and solid body rotation, respectively, symmetric and antisymmetric parts of the velocity gradient tensor $\nabla \mathbf{v}$. Obviously, pure rotation of the fluid is unable to provoke any bead collisions. Therefore, the relative

velocity is only a consequence of a local rate of deformation. This velocity gradient may be multiplied by the typical distance corresponding to the contact of two beads, i.e the bead diameter. A bead diameter $d_{GM} = \Delta R / 37.5$ has been chosen. Considering dimensions reported in Table 1, it corresponds to $d_{GM} = 400 \mu\text{m}$. It means that collision velocities between grinding beads in the mill are supposed to be modelled by relative velocities between spheres moving under the flow of the equivalent fluid. The magnitude of the velocity gradients can be obtained using the flow fields of the previous section and by calculating the eigenvalues of the strain rate tensor S (defined by Eq. (8)). The eigenvalues of the three-dimensional deformation rate tensor multiplied by the bead diameter give a measure of the local relative velocities. The local rotation of the flow is given by the rotation rate tensor Ω defined by

$$\Omega = \frac{1}{2}(\nabla \mathbf{v} - \nabla^t \mathbf{v}) \quad (13)$$

The type of collisions, frontal or oblique is related to the flow kinematics (S and Ω). Indeed, if the magnitudes of the deformation and rotation rate are similar it means that the collisions will be shear-induced. Shear flow is a particular combination of rotation and deformation rates with equal magnitude. On the contrary, if the magnitude of the eigenvalues of the deformation tensor dominate, collisions will be frontal.

The physics of liquid-solid suspensions is complex and the collision of solid particles embedded in a viscous fluids is a central mechanism in the comminution process. Particles are trapped in the active volume between two grinding beads experiencing an impact. The available kinetic energy for breaking fine particles is depending on the hydrodynamic regime of the collision. This can be mainly characterized by two non-dimensional numbers, namely the collisional Reynolds Re_{coll} and Stokes St_{coll} numbers. The Reynolds

number is based on the viscosity of the particle suspension μ_{susp} , the density of the particle suspension ρ_{susp} , the relative velocity ΔU between two grinding beads separated by the bead diameter d_{GM} .

$$Re_{coll} = \frac{d_{GM}\rho_{susp}\Delta U}{\mu_{susp}} \quad (14)$$

This will help to identify if the relative motion between the spheres is dominated by viscous or fluid inertia effects. The Stokes number compares two time scales: the viscous relaxation time of the bead and the characteristic time based on the collision velocity $R_{GM}/\Delta U$. The viscous relaxation time can be approximated using Stokes drag by $m_{GM}/3\pi\mu_{susp}d_{GM}$ where m_{GM} is the mass of a grinding bead. Therefore, after rearrangement, the Stokes number is:

$$St_{coll} = \frac{d_{GM}\rho_{GM}\Delta U}{9\mu_{susp}} \quad (15)$$

In general, the value of the impact Stokes number may vary from few hundreds in gas-solid suspension leading to elastic collisions (often termed as dry collisions) to less than unity for collisions of beads in viscous liquids. The critical Stokes number characterizing the occurrence of a rebound is in the range of 10–15 according to Gondret et al. (2002) and Legendre et al. (2006). Below this critical value the fluid dissipates all the kinetic energy of the relative motion and the beads do not bounce. Therefore, in the context of grinding in a stirred media mill, we expect collisional Stokes numbers significantly larger than the critical value for rebound meaning that if the collisions occur energy will be still available for breakage of the feed particles.

4.3. Maximum relative velocity and stress intensity in Newtonian fluids

The first stage of the analysis consists in estimating the maximum impact velocity in the whole domain without distinction of the type of collisions (frontal or oblique collisions). This will give the order of magnitude of the kinetic energy available for the comminution process. The maximum of the relative velocities ΔU does not follow a constant evolution with the Reynolds number due to the complex nature of the flow. We obtained approximately 5% of the velocity at the disc tip $V_{\theta}(r=R_d)$ for Newtonian flows, corresponding roughly to 0.3 m/s when the Reynolds numbers ranges between 229 and 654. These values agree with the relative velocities found experimentally in Mende (2005) which range from 0.2 to 5 m/s. Similarly, the kinetic energy of all collisions has the same trend and reaches a maximum of 3.2×10^{-6} J (calculated with ρ_{eff}). This value may appear very low but actually more than 75% of the domain corresponds to impact velocities lower than 1% of $V_{\theta}(R_d)$.

Kwade et al. (1996) proposed to scale the intensity of collisions by the reference stress intensity SI_{ref} defined as

$$SI_{ref} = \rho_{GM}d_{GM}^3V_{\theta}^2 \quad (16)$$

SI_{ref} is proportional to the maximum kinetic energy of the beads. It provides a scaling for the maximum energy available in the comminution process. Multiplied by a stress number SN which evaluates the number of efficient collisions (corresponding at least to the capture of one particle), we can estimate the energy available for breaking particles, called specific energy E_s . According to Kwade and Schwedes (1997), Stenger et al. (2005b), the stress intensity SI determines the size of the product particles for a given E_s . Indeed a decrease of SI , related to a smaller bead diameter for example, induces an increase of the contact number and then an increase of SN (and vice versa). SI and SN control the process performance. Optimal values of SN and SI exist: too many

collisions at low energy are unable to break particles and also few contacts at high energy are poorly efficient.

Based on the determination of ΔU , it is now possible to evaluate the stress intensity number SI defined below in which the disc tip velocity has been replaced by the maximum relative velocity between two neighbouring beads:

$$SI = \rho_{GM}d_{GM}^3\Delta U^2 \quad (17)$$

In the Figs. 12a, b and c we show the contours of stress intensity levels scaled by the reference stress intensity SI_{ref} given by 16. For clarity, SI/SI_{ref} values have been multiplied by a constant factor 10^3 as their maximum values ranges between 2.2×10^{-3} and 3.1×10^{-3} . Typically, $SI/SI_{ref} = 9 \times 10^{-4}$ corresponds to a shear rate of 1000 s^{-1} . Consequently, SI_{ref} is 3 orders of magnitude larger than the effective stress intensity involved in the collision. Two main areas of high intensity appear again near the disc and along the chamber wall where velocity gradients are the most intense. It is also correlated to the spatial distribution of the viscous dissipation rate because collisions are mainly related to

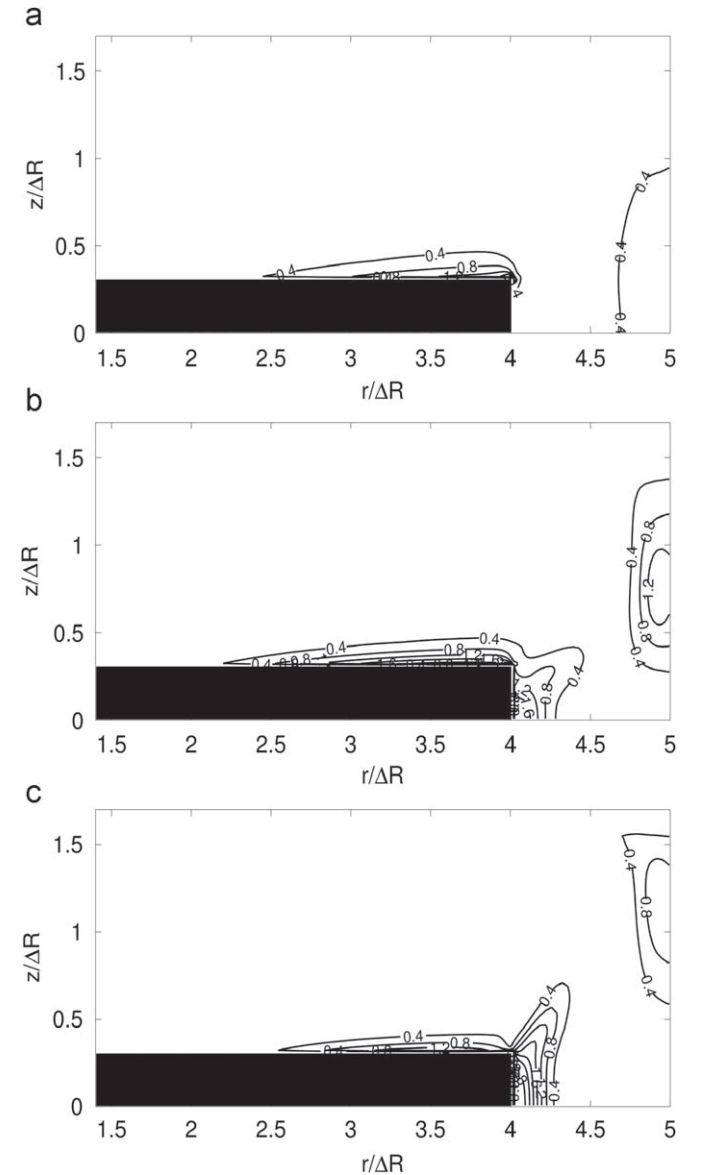


Fig. 12. Contour levels of $10^3 SI/SI_{ref}$ for a Newtonian fluid, for $Re = 229$ (a), $Re = 458$ (b), $Re = 654$ (c) from top to bottom.

the presence of shear flows. Indeed the first area, limited by the 0.4-isoline for example, expands and moves toward the disc tip when the Reynolds number is increased from 229 to 458. Between Reynolds numbers 458 and 654, this zone shrinks and moves toward the symmetry axis between the two discs close to the disc tip while the maximum value increases revealing that localized collisions are very intense for a Reynolds number equal to 654. On the contrary, the second area which moves toward the symmetry axis between two discs reduces as the Reynolds number increases (the maximum of the scaled stress intensity reaches a maximum for $Re = 458$).

Finally, the maximum relative velocity in the (r, z) plane is calculated in the simulation based on the eigenvalues of the deformation tensor S . The maximum values range from 3% to 3.5% of the tangential velocity at the disc tip $V_\theta(r = R_d)$. Therefore, secondary flows may play an important role in the comminution process. Also, they allow particles to move through areas of high shear rate in the gap between the chamber wall and the disc tip where particles are milled due to strong gradients of the tangential velocity.

4.4. Maximum relative velocity and stress intensity in non-Newtonian fluids

4.4.1. Shear-thinning fluids

Contour levels of the stress intensity SI for two shear thinning fluids are presented on Figs. 13a ($Re = 422$) and 13 b ($Re = 845$). Similarly to Newtonian fluids, the area of intense stress intensity near the disc develops at the disc tip and reduces along the disc wall when the Reynolds number is increased from 422 to 845. The area of high SI/SI_{ref} at the chamber wall moves from the gap between the chamber wall and the disc tip to the symmetry axis between the two discs. We observe that the ratio SI/SI_{ref} is higher in both simulations than for the Newtonian cases (maximum value 7×10^{-3} for $Re = 422$ and 4.1×10^{-3} for $Re = 845$). Therefore, collisions are expected to be more intense around the disc. Maximum relative velocities range between 8.35% (0.5 m/s) and 6.44% (0.39 m/s) of V_θ , respectively, whereas they reach 5.52% and 3.14% of V_θ if we restrict the analysis to the (r, z) plane. Compared to the simulations with a Newtonian fluid, secondary flows are less efficient in the comminution process when the Reynolds number is increased. The ratio between the total energy available for breakage and its related value solely to the secondary flows varies from 4 to 9 when the Reynolds number evolves between 422 and 845. Finally, it is interesting to note that the increase of the Reynolds number makes both areas of high stress intensity smaller. Indeed, relative velocities are lower than 1% of V_θ in 75% (for $Re = 422$) and 83% (for $Re = 845$) of the simulation domain.

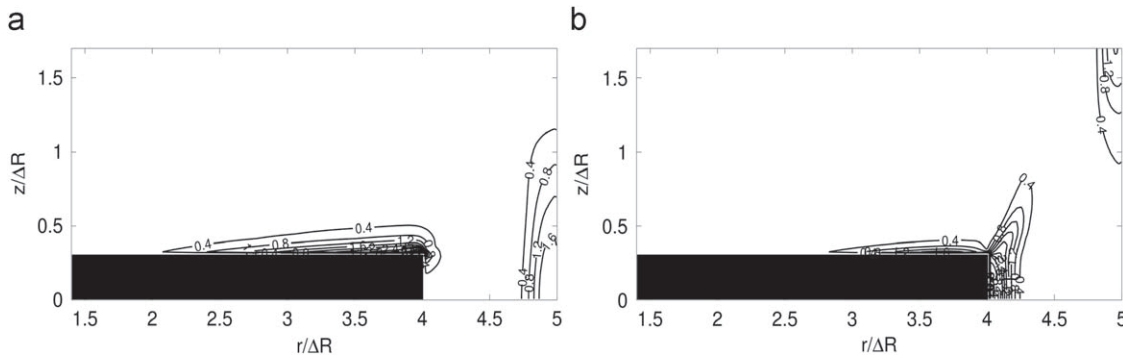


Fig. 13. Contour levels of $10^3 SI/SI_{ref}$ for a shear thinning fluid, for $Re = 422$ on the left (a), $Re = 845$ (b) on the right.

4.4.2. Shear-thickening fluid

Contour levels of $10^3 SI/SI_{ref}$ for a shear-thickening fluid are reported in Fig. 14 corresponding to $Re = 67$. The maximum values ($10^3 SI/SI_{ref} > 0.1$) are confined in a very narrow area between the disc tip and the chamber wall. The maximum of SI/SI_{ref} reaches 0.87×10^{-3} which is much smaller than those obtained for the other fluids. Indeed the maximum relative velocity is only 2.96% of V_θ (0.18 m/s) and 1.72% when we restrict the analysis to the (r, z) plane. That can be explained by the high viscosity of the equivalent suspension. Consequently, the energy of collision in the mill is weak (1×10^{-6} J). The ratio comparing the total available energy to the corresponding energy with the secondary flows in the (r, z) plane is now 9.3.

4.5. Prediction of colliding conditions

We stressed in Section 4.2 that St_{coll} and Re_{coll} help describing the hydrodynamic interactions of two grinding beads colliding. Both non-dimensional numbers depend mainly on the relative velocities of the beads ΔU (described in the previous section) and on the dynamic suspension viscosity μ_{susp} . μ_{susp} must be distinguished from the effective suspension viscosity μ_{eff} . Indeed, the collision between two beads occurs in a suspension of particles. The colliding beads are experiencing the effect of an effective surrounding media composed only with the carrying fluid and the particles (viscosity μ_{susp} , see Section 2.3). Therefore we can estimate maximum St_{coll} and Re_{coll} for beads of $400 \mu m$ diameter (6000 kg/m^3 for ZrO_2 beads) based on the value of μ_{susp} . In Table 3, we report the values of St_{coll} and Re_{coll} corresponding to each flow configuration characterized by Re (Eq. 9) and fluid nature.

St_{coll} and Re_{coll} are lower than the values measured for inertial particles experiencing actual rebounds. St_{coll} is below the critical

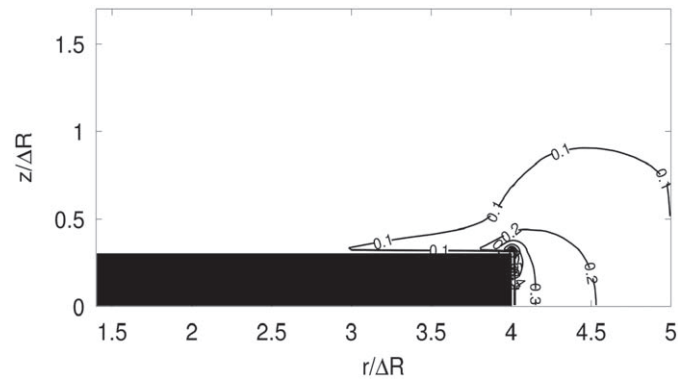


Fig. 14. Contour levels of $10^3 SI/SI_{ref}$ for a shear thickening fluid, $Re = 67$.

Table 3
Characteristic St_{coll} and Re_{coll} deduced from the simulations.

Fluid type	Re	ΔU (m/s)	μ_{susp} (Pa s)	St_{coll}	Re_{coll}
Newtonian	229	0.31	0.274	0.30	0.6
	458	0.28	0.137	0.55	1.1
	654	0.34	0.096	0.95	2
Shear-thinning	422	0.50	0.173	0.77	1.8
	845	0.39	0.086	1.21	2.7
Shear-thickening	67	0.18	0.688	0.07	0.05

value meaning that, if a collision occurs, the energy available for this collision will be mainly dissipated in the fluid during the near field hydrodynamic interactions. Moreover, based on the Re_{coll} values, fluid inertia and viscosity effects are of the same order. Probably, a higher rotation rate of the shaft would increase the values of St_{coll} and Re_{coll} for the same bead diameter.

Based on these results, we can assume that particles breakage is not forced by binary bead-bead collision but more likely by collective compression and friction. Indeed, St_{coll} being lower than the critical value of rebound, beads are experiencing long time enduring contacts favourable to attrition of the particles. Working at high concentration and high rotation frequency is advantageous while centrifugal force will induce the presence of high pressure zones in the flow.

5. Conclusion

The local hydrodynamics in a stirred media mill have been investigated by means of numerical simulations. The characteristic Reynolds number and the nature of the equivalent fluid (Newtonian or power law fluids) have been largely varied. We showed the existence of secondary flows constituted by several vortices of different sizes. These flows originate from a centrifugal instability due to the rotation of the discs. The effect of a weak axial flow is negligible on the flow structure compared to the strong rotation of the discs. We observed an increase of the viscous dissipation rate with the generalized Reynolds number (varying from 67 to 845). Although secondary flows and the mean axial flow are much less energetic than the tangential flow, they are very useful to mix the suspension. The particles of the suspension move through all the zones of high shear rates where they are broken by the contacts of grinding beads induced by strong velocity gradients. As Cleary et al. (2006) and Sinnott et al. (2006), we found that the energy consumption and particle agitation controlling the efficiency of milling is confined in very narrow areas close to the moving parts of the agitators.

The main contribution of this study is an original method to estimate impact velocities from the velocity fields. This information is a keystone in understanding the mechanisms occurring during the collision of two grinding beads. We modelled the suspension as a non-Newtonian fluid and investigated the evolution of the velocity gradients. Maximum relative velocities are obtained by computing the eigenvalues of the deformation rate tensor. Therefore, we determined effective impact parameters. Based on this analysis, we showed that collisions induced by the strong shear in the disc plane (r, θ) are the most intense and as a consequence the most efficient for the fragmentation of suspended particles since the plane (r, z) contains a low part of the total energy of collision and frontal collisions cannot occur in the plane (r, θ) because of purely azimuthal flow. In tower or pin mills, Cleary et al. (2006) and Sinnott et al. (2006) found also that collisions induced by the strong shear are the most efficient for the fragmentation. Nevertheless, the corresponding maximum velocities reach approximately 10% of the tangential velocity at the disc tip.

Finally, based on these estimations of impact velocities, the physical nature of the collision between two grinding beads have been analysed. The simulations predict the existence of low impact Stokes number showing no bead-bead rebounds. The velocity scale of the secondary flows is in the range of 10% to 25% of the tangential velocity of the discs. These flows in the (r, z) plane do not induce strong velocity gradient. On the other hand, the equivalent fluid sheared with the gap between the disc tip and the chamber wall experiences much stronger gradient (r, θ plane), typically $V_{\theta}/\Delta R = 6/0.015 = 400 \text{ s}^{-1}$. Although the shear rate is high, due to the small size of the beads, the relative velocity is weak (10% of the typical disc tangential velocity) and collisions without rebound are more likely to occur. This was an unexpected result. On the contrary, if we found that collisions in the fluid are almost elastic (weak dissipation by hydrodynamic interactions) this would contradict the assumption that bead velocity can be estimated by a one-fluid approach while a strong agitation of the beads would exist.

So, the milling of particles must be the result of compression and attrition generated by the friction of layers of grinding beads. We have evaluated the respective contributions of both mechanisms. In our simulations, the tangential stress (related to attrition by friction of neighbouring layers) is at least one order of magnitude larger than the compressive force (especially in the vicinity of the mill walls).

Acknowledgements

We are very grateful for the support of the National Research Agency under the programme ACI-Nanobroyage, the local support of the cooperative structure of joint research FERMAT and the regional high-performance computing centre CALMIP.

References

- Barnes, H.A., 1989. Shear-thickening ('dilatancy') in suspensions of non-aggregating solid particles dispersed in Newtonian liquids. *J. Rheol.* 33, 329–366.
- Barnes, H.A., Hutton, J.F., Walters, K., 1989. *An Introduction to Rheology*. Elsevier, Amsterdam, pp. 128–131.
- Bernhardt, C., Reinsch, E., Husemann, K., 1999. The influence of suspension properties on ultra-fine grinding in stirred ball mills. *Powder Technol.* 105, 357–361.
- Bernotat, S., Schönert, K., 1988. *Ullmann's Encyclopedia of Industrial Chemistry*, fifth ed VCH Verlagsgesellschaft, Weinheim (Chapter 5).
- Blecher, L., Schwedes, J., 1996. Energy distribution and particle trajectories in a grinding chamber of a stirred media mill. *Int. J. Miner. Process.* 44–45, 617–627.
- Blecher, L., Kwade, A., Schwedes, J., 1996. Motion and stress intensity of grinding beads in a stirred media mill. Part 1: energy density distribution and motion of single grinding beads. *Powder Technol.* 86, 59–68.
- Chhabra, R.P., 2003. Fluid mechanics and heat transfer with non-Newtonian liquids in mechanically agitated vessels. *Adv. Heat Transfer* 37, 77–178.
- Cleary, P.W., Sinnott, M., Morrison, R., 2006. Analysis of stirred mill performance using DEM simulation: part 2 coherent flow structures, liner stress and wear, mixing and transport. *Miner. Eng.* 19 (15), 1551–1572.
- Climent, E., Simonnet, M., Magnaudet, J., 2007. Preferential accumulation of bubbles in Couette–Taylor flow patterns. *Phys. Fluids* 19, 083301.
- Frances, C., Anne-Archard, D., 2004. Propriétés physiques de suspensions denses de particules microniques obtenues par nanobroyage en voie humide. 4ième Colloque Sciences et Technologie des poudres 4-6 Mai, Compiègne, France, Récents progrès en Génie des Procédés, 91 ISBN 2-910239-65-9.
- Garcia, F., Le Bolay, N., Trompette, J.L., Frances, C., 2004. On fragmentation and agglomeration phenomena in a ultrafine wet grinding process: the role of polyelectrolyte additives. *Int. J. Miner. Process.* 745, 543–554.
- Gondret, P., Lance, M., Petit, L., 2002. Bouncing motion of spherical particles in fluids. *Phys. Fluid* 14 (n^2), 643–652.
- Gudin, D., Kano, J., Saito, F., 2007. Effect of the friction coefficient in the discrete element method simulation on media motion in a wet bead mill. *Adv. Powder Technol.* 185, 555–565.
- Jayasundara, C.T., Yang, R.Y., Guo, B.Y., Yu, A.B., Rubenstein, J., 2009. Effect of slurry properties on particle motion in IsaMills. *Miner. Eng.* 22, 886–892.
- Kwade, A., Blecher, L., Schwedes, J., 1996. Motion and stress intensity of grinding beads in a stirred media mill. Part 2: stress intensity and its effect on comminution. *Powder Technol.* 86, 69–76.

- Kwade, A., Schwedes, J., 1997. Wet comminution in stirred media mills. *KONA*, 15.
- Kwade, A., 1999. Determination of the most important grinding mechanism in stirred media mills by calculating stress intensity and stress number. *Powder Technol.* 105, 382–388.
- Lane, G.L., 1999. CFD modelling of a stirred bead mill for fine grinding. Second International Conference on CFD in the Minerals and Process Industries CSIRO, Melbourne, Australia, 6–8 December.
- Legendre, D., Magnaudet, J., 1998. The lift force on a spherical body in a viscous linear shear flow. *J. Fluid Mech.* 368, 81–126.
- Legendre, D., Magnaudet, J., Mougou, G., 2003. Hydrodynamic interactions between two spherical bubbles rising side by side in a viscous liquid. *J. Fluid Mech.* 497, 133–166.
- Legendre, D., Zenit, R., Daniel, C., Guiraud, P., 2006. A note on the modelling of the bouncing of spherical drops or solid spheres on a wall in viscous fluid. *Chemical Engineering Science* 61, 3543–3549.
- Magnaudet, J., Rivero, M., Fabre, J., 1995. Accelerated flows past a rigid sphere or a spherical bubble. Part 1. Steady straining flow. *J. Fluid Mech.* 284, 97–135.
- Mende, G., 2005. Das Einfangen von Mahlgutpartikeln durch Mahlkugeln. Dissertation, T.U. Braunschweig.
- Mende, S., Stenger, F., Peukert, W., Schwedes, J., 2003. Mechanical production and stabilization of submicron particles in stirred media mills. *Powder Tech.* 132, 64–73.
- Merisko-Liversidge, E., Liversidge, G.G., Cooper, E.R., 2003. Nanosizing: a formulation approach for poorly-water-soluble compounds. *European Journal of Pharmaceutical Sciences* 18, 113–120.
- Mori, H., Mio, H., Kano, J., Saito, F., 2004. Ball mill simulation in wet grinding using a tumbling mill and its correlation to grinding rate. *Powder Tech.* 143–144, 230–239.
- Nagata, S., 1975. *Mixing, Principles and Applications*. Halsted Press, Wiley, New York.
- Sinnott, M., Cleary, P.W., Morrison, R., 2006. Analysis of stirred mill performance using DEM simulation: Part 1 Media motion, energy consumption and collisional environment. *Minerals Engineering* 19 (15), 1537–1550.
- Shook, C.A., Rocco, M.C., 1991. *Slurry flow*. Butterworth-Heinemann, London.
- Stenger, F., Mende, S., Schwedes, J., Peukert, W., 2005a. The influence of suspension properties on the grinding behaviour of alumina particles in the submicron range in a stirred media mill. *Powder Tech.* 156, 103–110.
- Stenger, F., Mende, S., Schwedes, J., Peukert, W., 2005b. Nanomilling in stirred media mills. *Chemical Engineering Science* 60, 4557–4565.
- Theuerkauf, J., Schwedes, J., 1999. Theoretical and experimental investigation on particle and fluid motion in stirred media mills. *Powder Tech.* 105, 406–412.
- Theuerkauf, J., Schwedes, J., 2000. Investigation of motion in stirred media mills. *Chem. Eng. Technol.* 23, 203–209.
- Weller, K.R., Spencer, S.J., Gao, M.-W., Liu, Y., 2000. Tracer studies and breakage testing in pilot-scale stirred mills. *Minerals Engineering* 13 (4), 429–458.
- Yang, R.Y., Jayasundara, C.T., Yu, A.B., Curry, D., 2006. DEM simulation of the flow of grinding media in IsaMill. *Minerals Engineering* 19, 984–994.